Boundary-Layer Meteorol (2017) 162:117–142
DOI 10.1007/s10546-016-0185-2

RESEARCH ARTICLE

Sensitivity of Turbine-Height Wind Speeds to Parameters in Planetary Boundary-Layer and Surface-Layer Schemes in the Weather Research and Forecasting Model

Ben Yang[1,2] · Yun Qian[2] · Larry K. Berg[2] · Po-Lun Ma[2] · Sonia Wharton[3] · Vera Bulaevskaya[3] · Huiping Yan[2] · Zhangshuan Hou[2] · William J. Shaw[2]

Received: 7 October 2015 / Accepted: 21 June 2016 / Published online: 21 July 2016

Abstract We evaluate the sensitivity of simulated turbine-height wind speeds to 26 parameters within the Mellor–Yamada–Nakanishi–Niino (MYNN) planetary boundary-layer scheme and MM5 surface-layer scheme of the Weather Research and Forecasting model over an area of complex terrain. An efficient sampling algorithm and generalized linear model are used to explore the multiple-dimensional parameter space and quantify the parametric sensitivity of simulated turbine-height wind speeds. The results indicate that most of the variability in the ensemble simulations is due to parameters related to the dissipation of turbulent kinetic energy (TKE), Prandtl number, turbulent length scales, surface roughness, and the von Kármán constant. The parameter associated with the TKE dissipation rate is found to be most important, and a larger dissipation rate produces larger hub-height wind speeds. A larger Prandtl number results in smaller nighttime wind speeds. Increasing surface roughness reduces the frequencies of both extremely weak and strong airflows, implying a reduction in the variability of wind speed. All of the above parameters significantly affect the vertical profiles of wind speed and the magnitude of wind shear. The relative contributions of individual parameters are found to be dependent on both the terrain slope and atmospheric stability.

Keywords Parametrization schemes · Parametric sensitivity · Planetary boundary layer · Surface layer · Turbine-height wind speed · Weather Research and Forecasting model

Electronic supplementary material The online version of this article (doi:10.1007/s10546-016-0185-2) contains supplementary material, which is available to authorized users.

✉ Larry K. Berg
larry.berg@pnnl.gov

1 CMA-NJU Joint Laboratory for Climate Prediction Studies, Institute for Climate and Global Change Research, School of Atmospheric Sciences, Nanjing University, Nanjing, China

2 Pacific Northwest National Laboratory, P.O. Box 999, Richland, WA 99352, USA

3 Lawrence Livermore National Laboratory, Livermore, CA, USA

1 Introduction

Renewable energy resources, such as wind and solar power, are essential for the mitigation of climate change and sustainable energy production (Sims et al. 2007; Shaw et al. 2009). Because the wind-energy resource is geographically widely distributed (Lu et al. 2009), wind-generated electricity has experienced significant growth around the world (Pimentel et al. 2002; National Renewable Energy Laboratory 2008; International Energy Agency 2008; Musgrove 2010). Current wind farms attain their highest energy production (operating at their rated generating power) in periods of steady moderate wind speeds (typically between 13 and 25 m s^{-1}). Yet, wind speeds across the layer swept by a turbine rotor can exhibit significant variability, even on very short time scales (e.g., minutes to hours) (Marquis et al. 2011; Banta et al. 2013), and this affects the variability and ultimately the integration of wind power into the electric grid.

Wind-resource characterization and operational wind forecasting rely heavily on the accuracy of fine resolution (approaching 1 km) numerical weather prediction (NWP) models (Mahoney et al. 2012) that can realistically resolve the small-scale flow features (Marjanovic et al. 2014). Real-time or zero to 6-h predictions of wind power based on NWP models are of vital importance for the operation of wind farms, and forecast errors or uncertainties in hub-height wind speed can have serious financial implications (Marquis et al. 2011). An added complication is that wind turbines are frequently deployed in complex terrain, in part to take advantage of low-level flow forced by topography. Spatial heterogeneity in land-use type and elevation can induce complex orographic and thermodynamic influences on both the mean and turbulent flows within the planetary boundary layer (PBL).

Although current generation NWP models run at fine resolutions, they cannot explicitly resolve fine-scale details of the turbulent flow in the PBL. Therefore, process- or empirical-based parametrization schemes, including the PBL scheme and surface-layer scheme, are used to represent subgrid turbulence processes that are highly variable in space and time. Many PBL and surface-layer schemes have been developed and steadily improved over the past decades (e.g., Mellor and Yamada 1974; Hong et al. 2006; Pleim 2007; Nakanishi and Niino 2009; Hong 2010; Jiménez et al. 2012). However, simplifications and assumptions made in parametrization schemes contribute to model uncertainty (e.g., Berg and Zhong 2005; Steeneveld et al. 2008; Storm et al. 2009; Carvalho et al. 2012; Hu et al. 2010, 2013; García-Díez et al. 2013). Deficiencies in model representations of turbulence can lead to significant errors in the simulated wind speed within the PBL, including at heights spanning the wind turbine. These model deficiencies produce inaccurate predictions and cannot be addressed with data assimilation techniques alone (Banta et al. 2013). Drechsel et al. (2012) evaluated the turbine-layer (between 20 and 250 m above ground level) wind speeds predicted by the European Centre for Medium-Range Weather Forecasting model at various European sites, showing that the model had difficulties in predicting the wind speeds over the depth of the PBL throughout the day. Storm and Basu (2010) compared low-level wind fields simulated with four different PBL schemes used in the Weather Research and Forecasting (WRF) model and found that the PBL parametrizations require additional improvement to accurately simulate wind speed in the lower part of the PBL. Other model studies (e.g., Carvalho et al. 2012; Yang et al. 2013; Draxl et al. 2014) showed that the performance of different PBL and surface-layer schemes were dependent on meteorological background conditions, and no PBL parametrization scheme was significantly superior to others for all atmospheric conditions. Moreover, PBL and surface-layer schemes that are calibrated or validated using measurements or large-eddy simulation (LES) of cases with simple terrain may not be suitable for complex terrain cases (Marjanovic et al. 2014). Yang et al. (2013) evaluated the hub-height wind speeds and ramp events simulated by the WRF model using three different PBL schemes over the Columbia Basin region in the north-western USA. Their results showed that all three PBL schemes produced significant biases in the simulations of wind speed profiles and ramp events, and the largest differences among simulations were found during stable conditions associated with low-level jets.

Parametrization schemes applied within NWP models apply numerous tunable parameters, including those used for the PBL and surface layer (e.g., Nakanishi and Niino 2009; Nielsen-Gammon et al. 2010; Jiménez et al. 2012). The values of individual parameters are determined through a calibration process that typically involves using measurements at limited locations and times to determine their values. However, observations of sufficient quantity throughout the PBL are lacking because of the limitations of current observational techniques, and most of the uncertain parameters are estimated from LES based on a small number of idealized cases. Sensitivity analysis can be used to quantify model parametric uncertainty and sensitivity and to identify the processes in the model that make the largest contributions to the results.

To explore the entire high-dimensional parameter space, an effective sampling method is needed to determine the statistical distribution of model results for all possible value combinations (e.g., Hou et al. 2012; Yang et al. 2012, 2015; Ma et al. 2013; Guo et al. 2014; Wan et al. 2014; Boyle et al. 2015). The sensitivity analysis, such as variance decomposition analysis, uses the distributions of variables to quantify the contribution of each input parameter to the overall variability in an ensemble of simulations. For example, Nielsen-Gammon et al. (2010) tested the WRF model sensitivity to 10 parameters in the Asymmetrical Convective Model version-2 PBL scheme (ACM2; Pleim 2007) by conducting multiple sets of experiments, indicating that the most important parameters could be identified through the sensitivity analysis approach. Zhao et al. (2013) used the quasi-Monte Carlo (QMC) method and a surrogate model to examine the sensitivities of the top-of-the-atmosphere radiative fluxes to 16 parameters used in the Community Atmosphere Model version 5 (CAM5). Qian et al. (2015) compared two sets of simulation ensembles with perturbed parameters generated by different sampling algorithms to explore the parametric uncertainties in precipitation simulations in CAM5.

To our knowledge, there has been no such comprehensive parametric sensitivity study of the PBL and/or surface-layer parametrization schemes for wind-energy applications. It is not clear which parameters associated with the PBL and surface-layer parametrizations are most responsible for the uncertainty in the simulated turbine-height wind speed and ultimately wind power. It is also uncertain how parameter sensitivity varies in both time and space. In this study, we adopt a sensitivity analysis framework (Zhao et al. 2013) that integrates an exploratory sampling approach (i.e., the QMC method) and a surrogate model (i.e., generalized linear model) (McCullagh and Nelder 1989) analysis, in order to evaluate the sensitivity of WRF-simulated hub-height wind speeds to different PBL and surface-layer parameters over the diverse Columbia Basin region.

The paper is organized as follows: Sect. 2 describes the WRF model configuration and selected field sites within the study area. The investigated parameters, their uncertainty ranges, and the sensitivity analysis methodology are also introduced in Sect. 2. In Sect. 3 we analyze the impacts of different PBL and surface-layer parameters on the simulated turbine-layer wind speeds to identify the most influential parameters and examine the dependence of their sensitivity to the terrain slope and atmospheric stability. The underlying mechanisms of parameter impacts on the simulated wind speeds are also briefly explored. The main findings are summarized in Sect. 4.

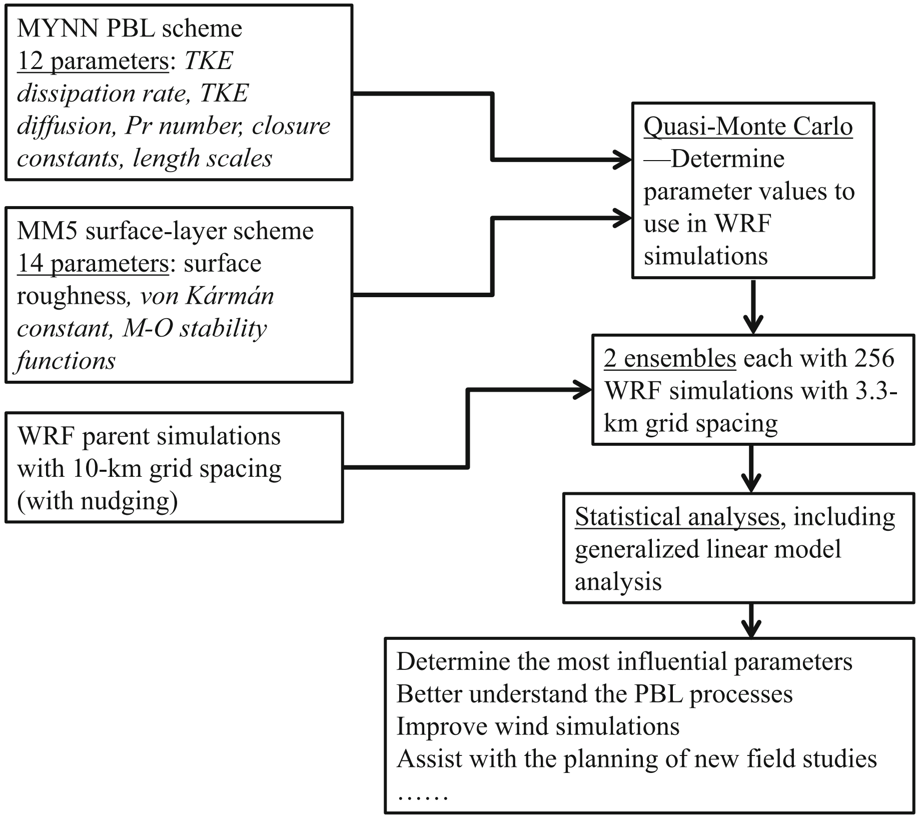

Fig. 1 Flow chart of the sensitivity analysis framework for WRF model simulations

2 Methodology

A sensitivity analysis framework (represented schematically in Fig. 1) that includes parameter sampling, model integrations, and statistical analysis, is applied to investigate the parametric sensitivity of the simulated wind speeds over the turbine-rotor layer. A total of 26 tunable parameters are selected from the Mellor–Yamada–Nakanishi–Niino (MYNN) PBL scheme and the MM5 (i.e., the fifth generation Pennsylvania State University–National Center for Atmospheric Research Mesoscale Model, Grell et al. 1994) Monin-Obukhov (M-O) scheme (Jiménez et al. 2012) surface-layer scheme. Two suites of 256 simulations using the WRF model are completed using a range of parameter values. Finally, the WRF model data are used as input to the generalized linear model that is utilized to determine the sensitivity of the simulated wind speed to variations in the parameter values.

2.1 Assumed Parameter Values

A total of 26 parameters are investigated, with 12 parameters associated with the MYNN PBL scheme and 14 with the revised MM5 surface-layer scheme. The relevant relations are briefly described in Online Resource 1. The choice of the parameters is based on a review of the existing literature, and from examining the equations in the parametrization schemes as applied in the WRF model. Once the parameters are selected, their ranges are determined based on values that have appeared in the literature for both the surface layer (e.g., Dyer 1967; Paulson 1970; Stull 1988; Fairall et al. 1996; Grachev et al. 2000; Cheng and Brutsaert 2005; Mass and Ovens 2010; Jiménez et al. 2012) and PBL schemes (e.g., Mellor and Yamada 1982; Kim and Mahrt 1992; Andren and Moeng 1993; Schumann and Gerz 1995; Nakanishi 2001; Nakanishi and Niino 2004, 2006, 2009; Grachev et al. 2007) or, in cases where no guidance is available, by increasing and decreasing the parameter value by a factor 0.5 and 1.5 times their default values. Because of the interdependencies among some of the parameters, we apply additional checks to ensure that values stay within realistic bounds, which leads to some modification of the ranges used. Specific values used for each of the parameters are described in the next sub-sections. The factors of 0.5 and 1.5 used for some variables are arbitrary, and a different range could have been applied. The comparison with data presented in Sect. 3 shows that the distributions of simulated and observed wind speed are quite similar, supporting the choice of ranges that have been selected. Likewise, using a different range is unlikely to result in the identification of a different set of key parameters.

2.1.1 PBL Parameters

The selected PBL parameters (Table 1, see Online Resource 1 for additional details) include those related to the turbulent kinetic energy (TKE) dissipation rate (B_1), TKE diffusion factor (D_f), the turbulent Prandtl number Pr, closure constants (C_2, C_5, and γ_1), and turbulent length-scale coefficients (α_1–α_5 and β in). The time evolution of TKE depends on the imbalance between its production and dissipation rate. In the WRF model the default value of B_1 related to the TKE dissipation rate is 24. The value of B_1 was estimated to be 16.6 by Mellor and Yamada (1982) and 27.4 by Andren and Moeng (1993) under neutrally-stratified conditions. Here the lower and upper bounds of B_1 are set to 12 and 36. Note that

Table 1 Investigated parameters in the MYNN PBL scheme

Parameter	Description	Default value	Estimated range
B_1	Constant for dissipation rate of TKE	24	[12, 36]
D_f (*sqfac*)	TKE diffusion factor	2	[1.5, 4.5]
Pr	Turbulent Prandtl number	0.74	[0.5, 2]
C_3	Closure constant	0.34	[0.33, 0.50]
C_5	Closure constant	0.2	[0.1, 0.3]
γ_1 ($g1$)	Closure constant	0.229	[0.1768, 0.2395]
α_1 (*alp1*)	Constant for calculation of the turbulent length scale (L_T)	0.23	[0.115, 0.345]
α_2 (*alp2*)	Constant for calculation of the turbulent length scale (L_B)	0.65	[0.5, 1.0]
α_3 (*alp3*)	Constant for calculation of L_B	3	[2.5, 7.5]
α_4 (*alp4*)	Constant for calculation of the turbulent length scale (L_S)	20	[20, 100]
α_5 (*cns*)	Constant for calculation of L_S	2.1	[1.35, 4.05]
β	Exponent on equation of L_S	0.2	[0.1, 0.3]

Note that the text in parentheses in the Parameter column is the name used for that parameter in the source code of the MYNN scheme in the WRF model the value of B_2 (Eq. 2 in Online Resource 1) is simultaneously adjusted with B_1 such that $B_2 = 0.625B_1$ (Mellor and Yamada 1982; Nakanishi 2001). The turbulent Prandtl number, *Pr,* (the ratio of the eddy diffusivity of momentum to that of heat) has a range in neutral or weakly stable conditions estimated between 0.7 and 1.2 by Schumann and Gerz (1995) and 0.5–2 based on the results of Kim and Mahrt (1992). Grachev et al. (2007) indicated that the upper limit of *Pr* could be 2 or 3. In the present study, a range of 0.5–2 is used for *Pr*. Nakanishi and Niino (2009) have pointed out that the range of C_3 should be between the theoretical values of 0.33 for isotropic turbulence and 0.5 for a convective boundary layer (Gibson and Launder 1978; Moeng and Wyngaard 1986). With the continued development of the MYNN model (Nakanishi 2001; Nakanishi and Niino 2004, 2009), the values of C_2 and C_3 have changed simultaneously several times, keeping a linear relationship between them. As a result, a range of 0.33–0.5 is used here for C_3 and the value of C_2 is determined using $C_2 = 1.724\,(C_3 - 0.323) + 0.7$, which is the relationship applied in the literature (e.g., Nakanishi and Niino 2009). The value of α_4 is 20 in the literature, but 100 in the WRF model source code, so we set a range of 20–100 for α_4. For $D_f, C_5, \alpha_1, \alpha_2, \alpha_3, \alpha_5$ and β, the uncertain ranges are set as 0.5–1.5 times their default values in the literature, except that the upper bound of α_3 is adjusted to 1.0 based on Nakanishi (2001).

In the MYNN PBL scheme, several closure constants are interconnected, and their values should stay within realistic ranges and should be of consistent sign when different values are applied for other parameters. For example, the values of A_1 and C_1 (Eqs. 5–7 in Online Resource 1) are expressed as functions of two independent parameters of B_1 and γ_1. In order to prevent A_1 or C_1 from being too small or large, their ranges are constrained in this analysis as 0.5^n–1.5^n (where n is the number of independent parameters) times their original values as B_1 and γ_1 are simultaneously perturbed. Given that the range of B_1 is assumed to be 12–36, it follows that the value of γ_1 should be within 0.1768–0.2395 instead of 0.5–1.5 times its original value so that the value of A_1 ranges from factors of 0.25 and 2.25 of its original value.

2.1.2 Surface-Layer Parameters

The selected surface-layer parameters (Table 2, further details can be found in Online Resource 1) include those used in the M-O stability functions (a_1–a_6 and b_1–b_6), surface-roughness scaling factor (z_f), and the von Kármán constant (k). Here z_f is used to define the surface roughness as $z_{new} = z_0 \cdot z_f$, where z_0 is the default surface roughness for each land-use type applied in the WRF model. For stable conditions, the values of a_1 and a_2 represent the slopes of similarity functions in weakly stable conditions. The ranges of a_1 and a_2 are set to 4.8–9.4 and 4.5–8.9 as estimated by Högström (1988). Cheng and Brutsaert (2005) stated that the stability functions for the wind-speed profile can also be applied to the temperature profile in stable conditions. As a result, the ranges of the exponents for the similarity functions for both momentum (i.e., b_1) and heat (i.e., b_2), are set from 1.1 (the original value for heat) to 2.5 (the original value for momentum) (Cheng and Brutsaert 2005). The ranges of a_5 and a_6 used in the similarity functions applied in convective conditions range between 9.7–11.6 and 26–42, respectively, which were estimated by Grachev et al. (2000) to match the Kansas-type or Businger–Dyer formulae (e.g., Izumi 1971; Dyer 1974; Businger 1988) when $a_3 = a_4 = 16$. It follows that the values of a_3 and a_4 cannot be much different from 16, so we set the ranges to 14–18 for both parameters. As shown in Eqs. 18, 19, 21, and 22 in Online Resource 1, the default values of the exponents (0.25 for momentum and 0.5 for heat, Table 2) based on the results from the Kansas field study (e.g., Izumi 1971) are replaced by 0.33 in the convective formulae. Because the ranges of a_3–a_6 are dependent on

Table 2 Investigated parameters in the revised MM5 surface-layer scheme. Note that ψ_m and ψ_h are the integrated similarity functions for momentum and heat

Parameter	Description	Default value	Estimated range
a_1	Constant associated with ψ_m at stable condition	6.1	[4.8, 9.4]
b_1	Exponent on equation of ψ_m at stable condition	2.5	[1.1, 2.5]
a_2	Constant associated with ψ_h at stable condition	5.3	[4.5, 9.0]
b_2	Exponent on equation of ψ_h at stable condition	1.1	[1.1, 2.5]
a_3	Constant associated with Kansas-type ψ_m at unstable condition	16	[14, 18]
b_3	Exponent on equation of Kansas-type ψ_m at unstable condition	4	[3.5, 4.5]
a_4	Constant associated with Kansas-type ψ_h at unstable condition	16	[14, 18]
b_4	Exponent on equation of Kansas-type ψ_h at unstable condition	2	[1.5, 2.5]
a_5	Constant associated with ψ_m at convective limit	10	[9.7, 11.6]
b_5	Exponent on equation of ψ_m at convective limit	3	[2.5, 3.5]
a_6	Constant associated with ψ_h at convective limit	34	[26, 42]
b_6	Exponent on equation of ψ_h at convective limit	3	[3.0, 3.5]
z_f	Scaling factor for surface roughness	1	[1.0, 2.0]
k	von Kármán constant	0.4	[0.35, 0.40]

the values of these exponents, it is unreasonable to choose ranges that are too wide for these exponents. Therefore, the ranges are set to 3.5–4.5 for b_3, 1.5–2.5 for b_4, and 2.5–3.5 for both b_5 and b_6. We found that large values of b_6 induce computational instabilities, so the range of b_6 is limited to be 2.5–3.0. The range of surface-roughness scaling factor z_f is set to 1–2 following Mass and Ovens (2010). The von Kármán constant k is used in both the PBL (Nakanishi 2001) and surface-layer (Jiménez et al. 2012) schemes; here k is grouped with the surface-layer parameters and its perturbed range is set to 0.35–0.4 (Stull 1988).

2.2 WRF Model Configuration

We focus on a region of complex terrain centered at the Columbia Basin Wind Energy Study (CBWES; Berg et al. 2012) field site, which is located on a north-east facing slope of an extensive ridge within the Stateline Wind Energy Center in Oregon, USA. CBWES included the deployment of a Vaisala, Inc., 915-MHz radar wind profiler [supplied by the U.S. Department of Energy's Atmospheric Radiation Measurement (ARM) Climate Research Facility], a Scintec MFAS Doppler sodar, and tower-mounted Applied Technologies, Inc., SATI/3K three-dimensional sonic anemometers to provide measurements of wind speed and direction over a large portion of the depth of the PBL (Berg et al. 2012). A number of

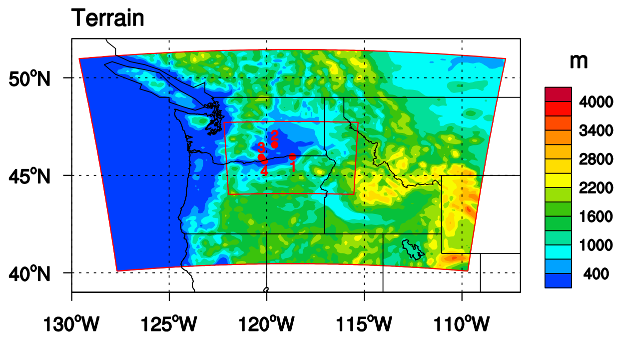

Fig. 2 Nested WRF model domains (*red boxes*) with 10-km and 3.3-km grid spacing, respectively. Terrain height is indicated by *colour* (see *legend* on the *right*). The *red dots* denote the locations of field measurements or wind plants used, including: *1* CBWES, *2* Hanford, *3* Big Horn, and *4* Pebble Springs

additional sites located within the Columbia Basin, including Hanford, Big Horn, and Pebble Springs, are also selected for analysis (Fig. 2). These particular locations are selected for comparison because of their proximity to wind farms and a wide range of different terrain, spanning simple to complex. Of these four locations, three (the CBWES, Big Horn, and Pebble Springs) are in or near existing wind farms. The Hanford site is located near the centre of the Columbia Basin.

The Advanced Research WRF model version 3.6 is used (Skamarock et al. 2008), utilizing two domains, one nested in the other (Fig. 2). The outer domain encompasses 40° to 52°N and 108° to 129°W with a 10-km grid spacing, and the inner domain covers 44° to 48°N and 115° to 122°W with a 3.3-km grid spacing. There are 150 grid points in the east-west direction and 120 grid points in the north-south direction for both domains. The terrain data with horizontal resolution of around 0.9 km are used and re-gridded to match the WRF model horizontal grid spacing. The model is configured with 55 layers using a vertical grid spacing of approximately 15 m in the lowest 200 m above ground.

Additional model physics packages that are applied including the Goddard shortwave radiation scheme (Chou and Suarez 1994) and the Rapid Radiative Transfer Model for long-wave radiation (Mlawer et al. 1997). The four-layer Noah land-surface model (Chen and Dudhia 2001) is chosen to represent the surface processes.

Boundary and initial conditions for the outer WRF model domain are derived from the North American Regional Reanalysis (NARR; Mesinger et al. 2006). Default parameter values are applied in the single set of WRF model simulations for the outer domain in which the wind speed and direction, temperature, and moisture are nudged to the NARR reanalysis. The model output from the outer domain is used as the initial and boundary conditions (i.e. nesting in offline mode) to drive the inner domain simulations that are performed repeatedly with the perturbed values for the parameters (see Sect. 2.3). This strategy helps to isolate the impacts of parameter perturbations within the inner domain (i.e. local impacts) from that of changes in boundary forcing. The WRF model is run from April 28 to May 31, 2011; the first three days are considered spin-up time and only the simulations from the month of May are used for parametric sensitivity analysis.

2.3 Sensitivity Analysis Framework

Following Zhao et al. (2013) and Guo et al. (2014), the QMC sampling approach (Caflisch 1998) is applied to uniformly sample points within the multi-dimensional parameter space. Simultaneously perturbing all 26 parameters would require a large number of samples and a huge amount of computational resources to obtain effective ensembles of model results. Instead, we apply a more economical approach by treating the PBL and surface-layer parameters as two individual groups and then sample the groups independently using the QMC algorithm. This strategy means that we are unable to investigate the effects of interactions between the PBL and surface-layer parameters. Given that the parameter sensitivity may vary when the parameter values in the other scheme are changed, the impact of some parameters may be underestimated here.

The number of samples required by the QMC method is normally a power of two to ensure a uniform sampling within the parameter space (Hou et al. 2012). Hou et al. (2012) found 128 samples were adequate to produce reliable results for a case with 10 parameters. Zhao et al. (2013) used 256 samples to explore the parametric sensitivity within a 16-dimensional space. Here, 256 parameter sets for each group are generated by the QMC method, and all the parameter sets (with parameters from the other group, either PBL or surface, fixed at their default values) are used in WRF model simulations configured as described in Sect. 2.1. A total of approximately 1.2×10^6 core hours were consumed to conduct these experiments.

The generalized linear model (McCullagh and Nelder 1989), which is introduced in Online Resource 2, is constructed using the simulation results. The generalized linear model is used to examine the parameter impacts by computing the variances of the model output variables (i.e., turbine-height wind speeds at different model grid points) associated with each individual parameter as well as the interaction among different parameters within either the PBL and surface-layer ensembles.

3 Results

In this section, we first analyze the impacts of different parameters on the simulated hub-height (i.e., 80-m) wind speed. The impacts on the simulated wind speed profile, wind shear, and turbulence characteristics are then investigated.

3.1 Turbine-Height Wind Speed

The ensemble of WRF-simulated wind speeds resulting from the perturbations of the PBL parameters provides a reasonable representation of the observed distribution of wind speed measured at the CBWES site (Fig. 3); this is particularly true for wind speeds <7.5 m s^{-1}. There is a tendency for the WRF model to overestimate the frequency of wind speeds between 9 and 11 m s^{-1}, and to underestimate the frequency for wind speeds greater than 11 m s^{-1}. Similar results were also found in simulations with a finer horizontal resolution presented by Yang et al. (2013).

Relatively small changes in the wind speed can lead to large variations in the generated wind power because of the nonlinear relationship between wind speed and wind power. When the wind speed is smaller than the cut-in wind speed of the turbine, typically around 3 m s^{-1}, the turbine remains nonoperational and no power is produced. Above the cut-in speed, power production increases as an approximately cubic function of the wind speed until reaching rated power, or a near-constant maximum power that is independent of the wind speed. Although the rated wind speed varies between turbine types, it is typically between 10 and 15 m s^{-1}. Turbines are shut down during periods very large wind speeds, called a cut-out speed, generally between 20 and 25 m s^{-1}, to avoid damage to the turbine components.

Wind power forecasts are generated based on a manufacture's power curve for a General Electric 1.68 MW turbine, assuming a hub-height of 80 m, rotor diameter of 82.5 m, and

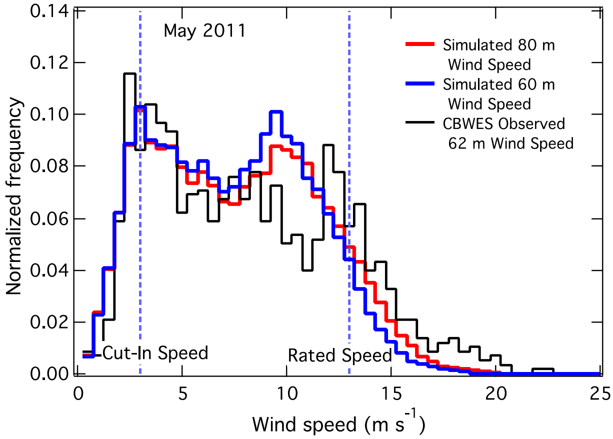

Fig. 3 Normalized frequency of observed wind speed at 62 m (*black*) and simulated wind speed at 60 m (*blue*) and 80 m (*red*) for cases with varying PBL parameters at the CBWES field site. *Vertical lines* indicated a typical turbine cut-in speed and rated speed

Fig. 4 Simulated time series of 80-m (*top*) wind speed and (*bottom*) wind power at CBWES in all the simulations with perturbed PBL parameters. *Black line* in the *top panel* indicates observed wind speed

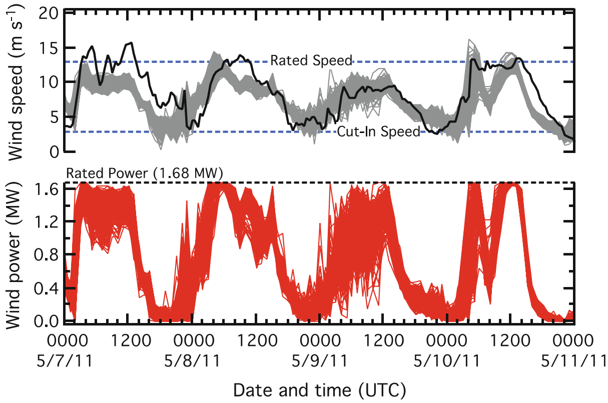

standard air density of 1.225 kg m^{-3}. For this turbine model, the cut-in speed is 3 m s^{-1}, rated speed is 13 m s^{-1} and cut-out speed is 25 m s^{-1}. The ensemble members generated with different PBL parameter values have different time evolution of wind speed, and hence wind power (Fig. 4), so that even small or moderate uncertainties in the wind speed can give rise to large uncertainties in the wind power ranging from very small values to the rated power of the turbine. For example, at 0600 UTC on May 9 2011 the uncertainty in wind speed led to power forecasts ranging from near zero (0.4 MW) to the rated power (1.68 MW).

3.1.1 Spatial Distribution of Parametric Sensitivity and Relation to Terrain Slope

The mean and variance between ensemble members (i.e. response to perturbed parameters) of 80-m wind speed vary as a function of both space and time of day (daytime vs. nighttime) over the study domain (Fig. 5). Wind speeds for each simulation are first averaged separately across daytime (0600–1800 LT) and nighttime hours (1800–0600 LT) at each grid point, and these daytime and nighttime averages for each individual simulation are in turn used to derive the simulation ensemble means and variances between ensemble members. The area of the

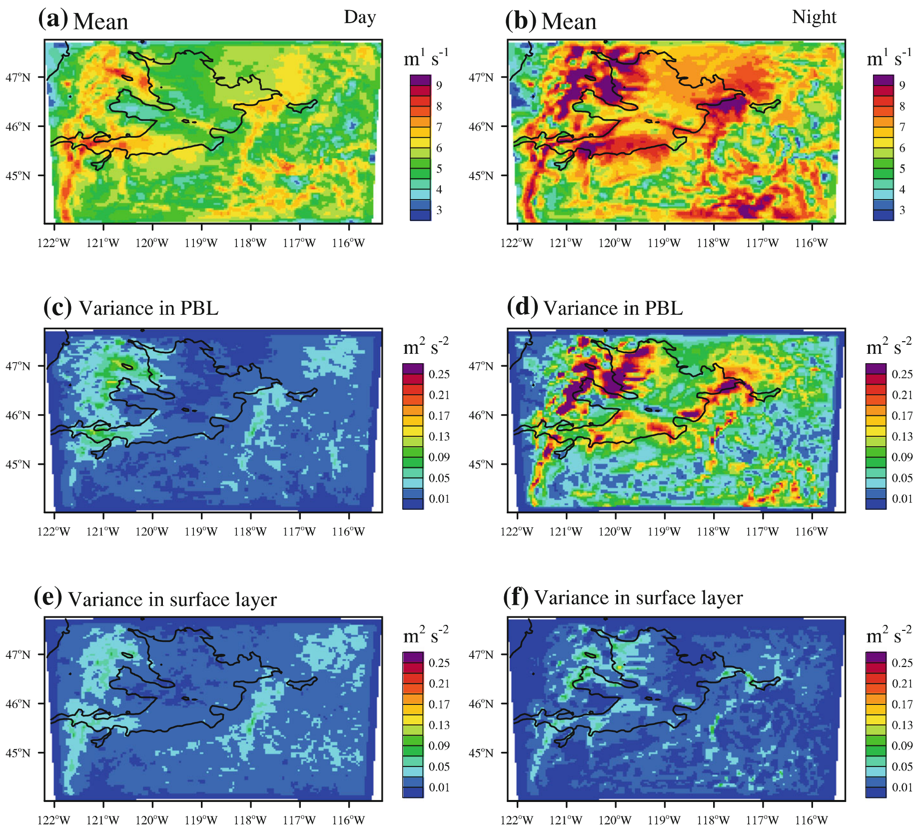

Fig. 5 Spatial distributions of simulation ensemble means computed using all the 512 simulations with perturbed PBL and surface-layer parameters (*top row*) and variances between ensemble members with perturbed PBL (*middle row*) and surface-layer (*bottom row*) parameters for the 80-m wind speed averaged separately across daytime hours (0600–1800 LT, *left*) and nighttime hours (1800–0600 LT, *right*). See text for details. Note that the means are not shown for PBL and surface-layer ensembles separately because they were found to be very similar to one another

domain where the terrain height is below 500 m, approximately representing the Columbia Basin, is marked in the plots. Compared to daytime conditions, nighttime domain-averaged wind speeds are much larger, with the maximum speed exceeding 9 m s^{-1}. Limiting the analysis to conditions over the basin, the average wind speeds during the simulation period range between 5.0–6.5 m s^{-1} during daytime and 6.5–8.5 m s^{-1} during nighttime.

The spatial patterns of the inter-simulation variances are well correlated with the simulation mean fields and, in general, the variances induced by parameter perturbations are larger at night (especially for PBL parameters), but there is some dependence of the variance on the terrain height. During daytime, the area with large variability in wind speed between ensemble members is limited to high elevation areas in the western part of the model domain, while the variability over the Columbia Basin is very small. On the contrary, the variability over the basin area is much larger during nighttime than daytime, which is likely because of the larger nighttime wind speeds found over the basin. The analysis highlights that the variability in the 80-m wind speed is much larger for the PBL parameters than is found for the surface-layer parameters, regardless of the time of day.

The generalized linear model (McCullagh and Nelder 1989) is used to decompose the total variances into the portions contributed by each of the different parameters as well as their interactions. Details of our implementation of the generalized linear model can be found in Online Resource 2. Our generalized linear model results indicate that the response of the 80-m wind speed is mainly caused by the individual effect of each parameter while the effects of the interactions of various parameters in the PBL and surface-layer schemes are negligible over much of the domain (not shown). Therefore, the generalized linear model results presented in this section are constructed by only considering the individual effect of each parameter (we fit linear and quadratic terms in each parameter as this was found to be sufficient to explain most of the variance in the output).

As shown from the generalized-linear-model estimated variances of 80-m wind speed, several PBL parameters are found to contribute more to the total variance of the ensemble than others, and some of the key parameters change with time of day (Figs. 6, 7). Note that the large value of the variance is found along the domain boundary in the α_1 plot (Fig. 6), which is likely associated with issues related to the boundary conditions at the edge of the WRF model nest. During daytime, the parameter B_1 (which is related to the TKE dissipation rate) is the most important parameter as it plays a key role in regulating the diurnal evolution of TKE, especially over high terrain region (Fig. 2) where changing B_1 contributes approximately 50 % of the total variance. The second most important parameter during daytime is found to be β (which is related to the turbulent length scale during unstable conditions), and its impact is more significant over areas with lower terrain within or close to the basin region. The effects of the other parameters are much smaller than those found for either B_1 or β, and the impacts induced by C_5, α_3 and α_5 are almost negligible during daytime. The relative contributions of B_1 and β to the generalized linear model estimated total variance of daytime 80-m wind speed at the CBWES site are 28 and 35 %, respectively, and the contributions of the other parameters are less than 15 % each.

Given that stable conditions are more common at night, we expect to see differences in the relative impact of parameters that are applied within the parametrization scheme as a function of stability. The importance of B_1 continues at night. In contrast, the parameter β has nearly no effect on the simulated 80-m wind speed at night because the turbulent length scale is not sensitive to β during stable conditions. In contrast, the importance of the parameter α_5 increases, especially over the basin region. The parameter Pr also moderately impacts the simulated 80-m wind speed during nighttime. The relative contributions of B_1, Pr and α_5 to the generalized linear model estimated total variance of nighttime 80-m wind speed at the CBWES site are 18, 38 , and 25 %, respectively.

An examination of Figs. 6 and 7 suggests that the impacts of different parameters on the simulated wind speed are dependent on the terrain height and/or slope. Figure 8 shows the relative contributions of each PBL parameter to the variances of the 80-m wind speeds as a function of terrain slope during both daytime (red) and nighttime (blue) conditions. Five grid points at each edge of the domain are excluded in the calculation to eliminate the contamination effects of nesting (Fig. 6). Similar to the evidence presented in Figs. 6 and 7, B_1 is found to have the largest impact on the simulated 80-m wind speed, with the mean contribution being between 30 and 50 %, depending on the slope and time of day. The diffusion factor D_f is much less important than B_1, and its impact has only a weak dependence on the terrain slope. The mean relative contribution of D_f is around 3 % during daytime, and 5 % during nighttime. The turbulent Prandtl number, Pr, contributes about 18 % of the total variance of the 80-m wind speed during nighttime. In daytime, its contribution is around 5 % for flat regions but above 10 % for regions with steep slopes. The variance explained by γ_1 is sensitive to the terrain slope during daytime,

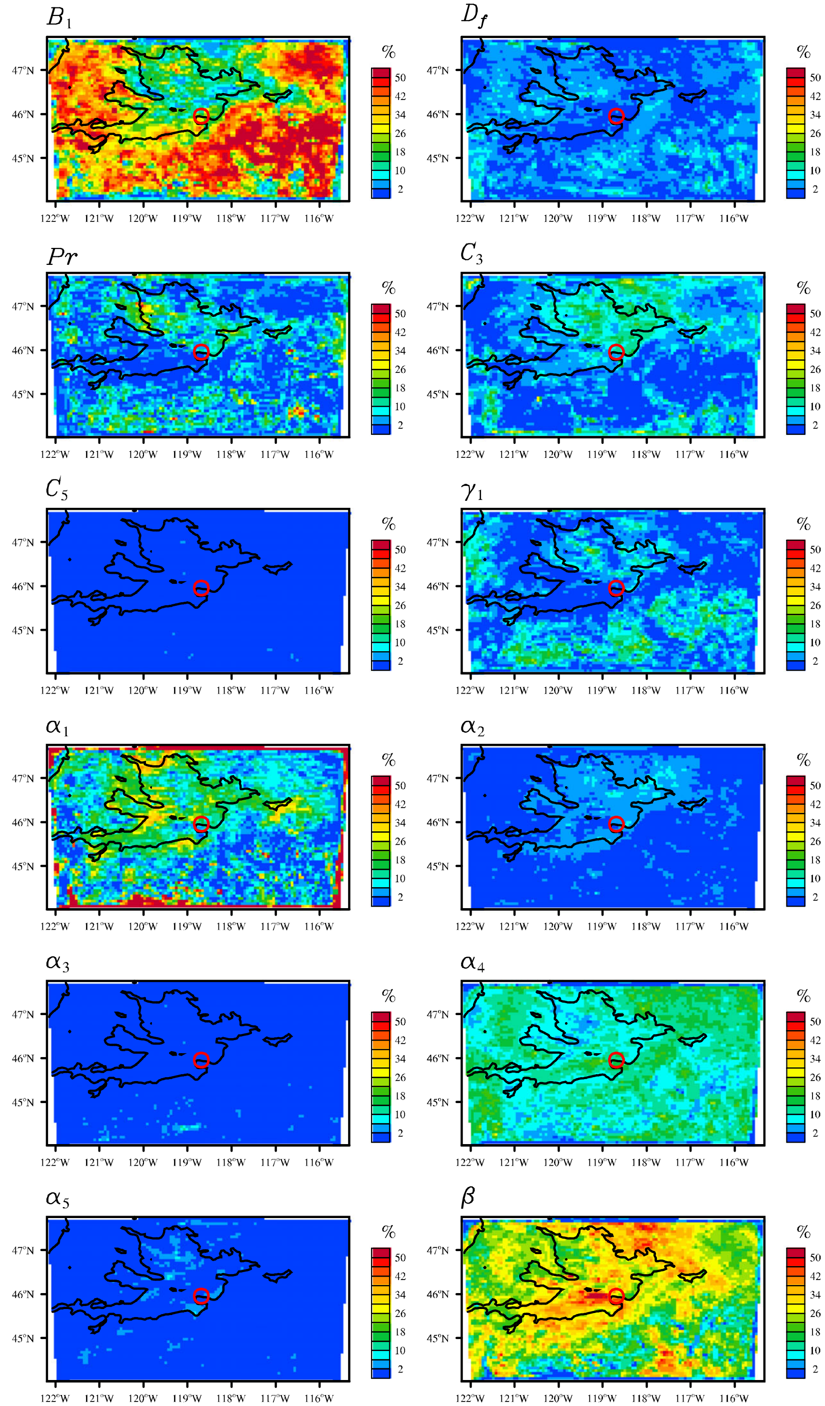

Fig. 6 Spatial distributions of relative contributions (in %) of each PBL parameter (Table 1) to the generalized linear model estimated total variances of the 80-m wind speed during daytime. The location of the CBWES site is marked by a *red circle* in each plot

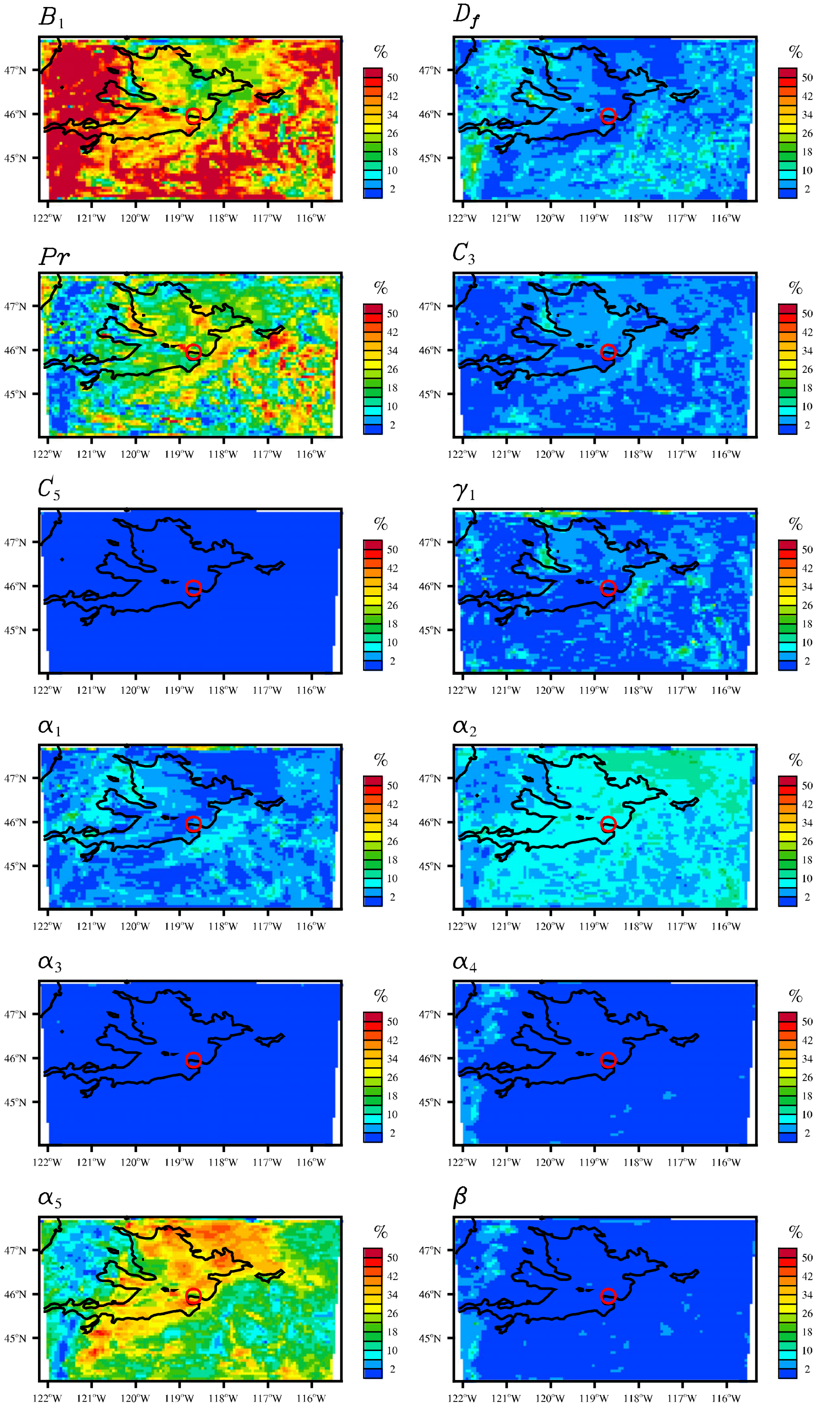

Fig. 7 Spatial distributions of relative contributions (in %) of each PBL parameter (Table 1) to the generalized linear model estimated total variances of the 80-m wind speed during nighttime. The location of the CBWES site is marked by a *red circle* in each plot

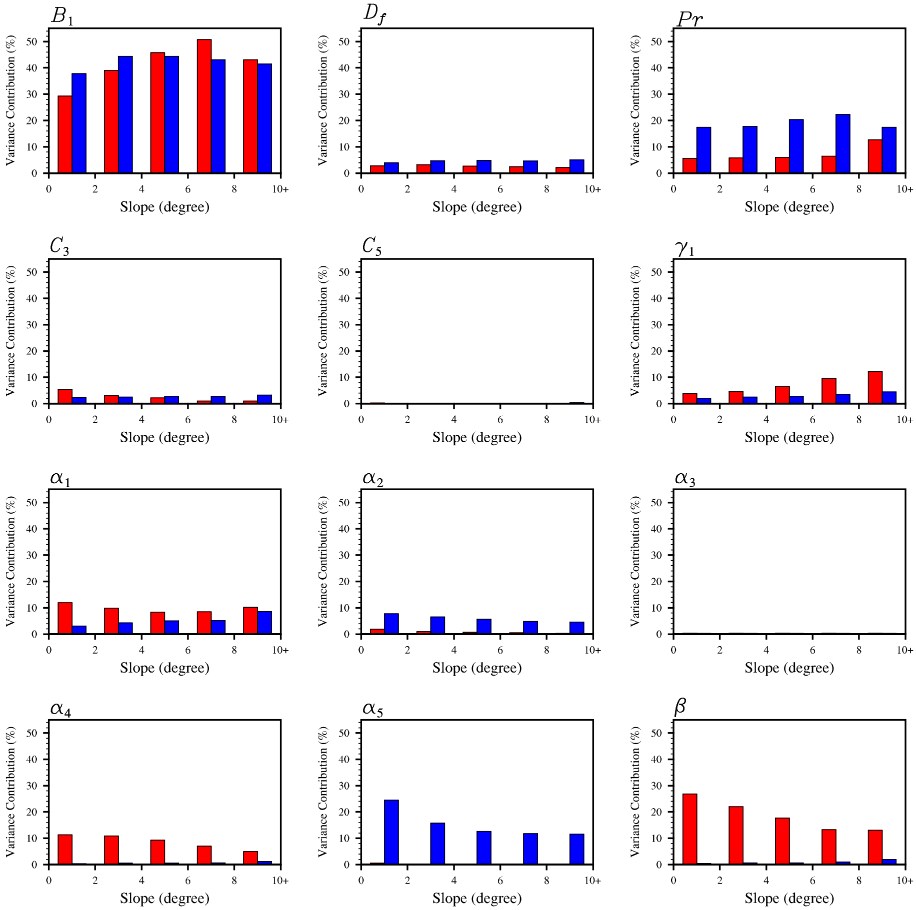

Fig. 8 Relative contributions of each PBL parameter to the variance of 80-m wind speed as a function of terrain slope during daytime (*red*) and nighttime (*blue*) conditions

with significantly larger contributions to the total variance over areas with steep slopes. A large portion of the variances in the 80-m wind speed can be attributed to the perturbations of the parameters related to the turbulent length scale applied in the MYNN parametrization scheme. For example, the parameter α_1 has considerable effects on the simulated wind speed during both daytime and nighttime conditions, as α_1 affects the turbulent length scale regardless of the stability (Eq. 11 in Online Resource 1). In contrast, the other parameters associated with the turbulence length scale only influence the simulated wind speed during either daytime or nighttime and not both, as their effects are a function of the stability. The values of α_2 and α_5 have large impacts on the variance during nighttime that is especially pronounced over areas with more gentle slopes. The parameters α_4 and β are found to significantly affect the daytime wind speed, and their impacts are also sensitive to the terrain slope. The relative contribution of β to the total daytime variance is about 26 % when the slope is less than two degrees and only 14 % for regions with slopes greater than six degrees, where the turbulent length scale is generally smaller because of the higher latent heat flux associated with larger amounts of vegetation at higher altitudes as found in this domain.

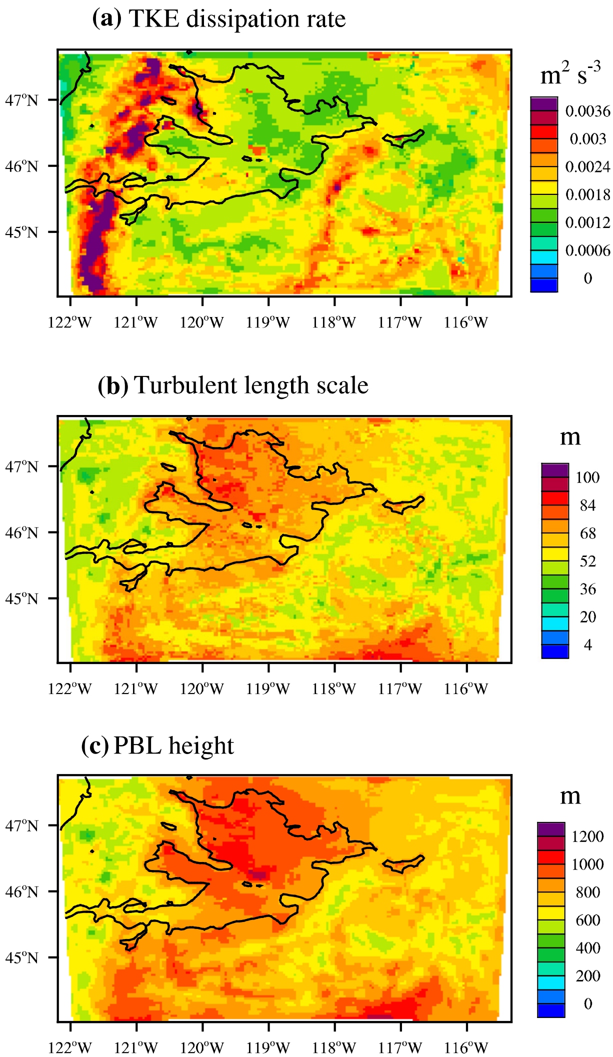

Fig. 9 Spatial distributions of simulation ensemble means computed using the 256 simulations with perturbed PBL parameters for TKE dissipation rate (**a**), turbulent length scale from the MYNN parametrization scheme (**b**), and PBL height (**c**) averaged during the day. Values for TKE dissipation rate and turbulent length scale are averaged within the lowest 1000 m layer

The sensitivity of the simulations to terrain slope is strongly influenced by the variation of the PBL properties across the domain (Fig. 9). For example, B_1 is less important over the basin region because the TKE dissipation rate is generally small over these areas (Fig. 9a). The spatial distribution of the turbulent length scale (Fig. 9b) is similar to that of the TKE dissipation rate because a larger turbulent length scale lead to smaller TKE dissipation rates (Eq. 1 in Online Resource 1). The large values of PBL height over areas with lower terrain (Fig. 9c) are responsible for large values of the turbulent length scale (Eqs. 9 and 11 in Online Resource 1) and thus small TKE dissipation rates. In addition, small values of the friction velocity over areas with low terrain (figure not shown) lead to small magnitudes of the Obukhov length (e.g. Nakanishi and Niino 2009; Jiménez et al. 2012) particularly during daytime, which further leads to large values of the turbulent length scale (Eqs. 9 and 10 in Online Resource 1). Given that the turbulent length scale is dominated by the smallest term among the variables L_S, L_T, and L_B (Eqs. 9–12 in Online Resource 1), this length scale is more sensitive to the changes in the surface length scale L_S over the basin region than over other regions where PBL height and L_T are small. Therefore, α_5 and β, which control L_S during nighttime and daytime, are more important over areas with simple terrain within the domain.

In summary, for the MYNN PBL scheme, the parameters B_1 and β are the most influential in regards to the daytime simulated 80-m wind speed, and B_1, Pr, and α_5 are the most influential during nighttime.

A similar analysis is performed for the surface-layer scheme parameters. In this case we find z_f and k jointly contribute more than 80 % of the total variance of the simulated wind speeds in the surface-layer ensemble over most of the domain. The spatial distributions of the relative contributions of z_f and k for the 80-m wind speeds are shown in Fig. 10. We find that during daytime, z_f contributes more than 50 % of the total variance at high elevations and about 40 % over the basin. The stronger impact of z_f at higher elevations is likely because of rougher terrain as well as taller and denser coverage of vegetation and thus larger surface roughness (not shown). In contrast, the value of k is more important over the basin region where it explains more than 50 % of the total variance. This is likely because the value of k is also used for the calculation of the surface length scale L_S, which plays a larger role for the change in the turbulent length scale over areas with simple terrain than over areas with complex terrain. Similar results are found for nighttime conditions except that the relative contributions of z_f and k are smaller and the impact of k is less sensitive to terrain than during daytime. This occurs because the parameters a_1 and b_1, which are related to the similarity function for momentum during stable conditions, become more important during nighttime,

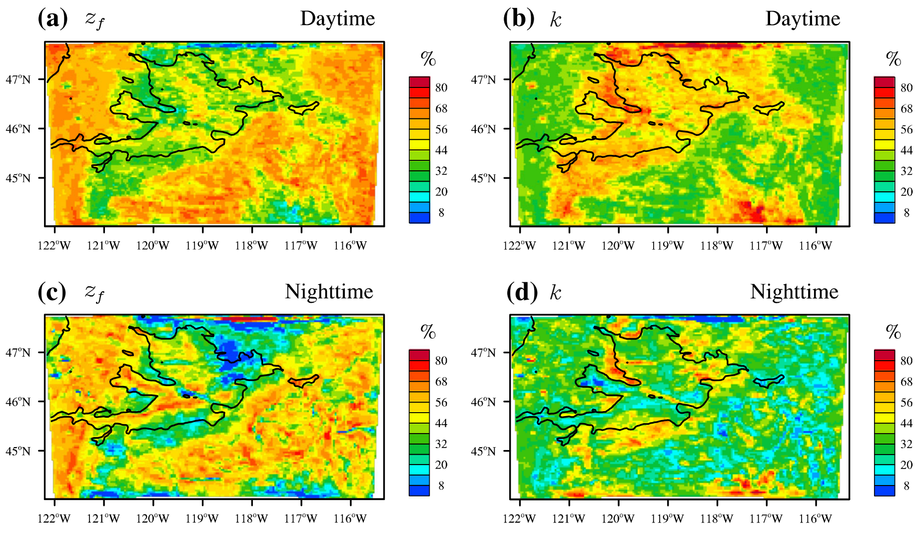

Fig. 10 Spatial distributions of relative contributions of z_f (**a**, **c**) and k (**b**, **d**) in the surface-layer scheme to the generalized linear model estimated total variances of the 80-m wind speed during daytime (**a**, **b**) and nighttime (**c**, **d**)

especially over areas of small terrain slope (Figure not shown),. However, the effects of a_1 and b_1 are still much weaker than those induced by z_f and k, even during nighttime.

3.1.2 Parametric Sensitivity at Select Locations

The responses to the perturbations of the six most influential parameters (i.e., B_1, Pr, α_5, and β in the PBL scheme and z_f and k in the surface-layer scheme, respectively), have been analyzed at the CBWES site and at Hanford, Big Horn, and Pebble Springs (locations are shown in Fig. 2). The results are consistent across the locations (Fig. 11). In each panel of Fig. 11, the deviation from the ensemble mean associated with changing parameter values in the 256 simulations have been placed into eight discrete bins (each bin with 32 experiments) based on the value of the parameter value. The mean differences of the simulated wind speeds among the bins (associated with values of the parameter ranging from the smallest to largest) are caused by the perturbation of a given parameter value displayed along the X-axis, while the range within each bin is induced by the interactions of the other parameters in each simulation ensemble. For example, B_1 is allowed to vary between 12 and 36, and thus the first box-and-whisker set in the top left corner of Fig. 11 shows the model deviation when values of B_1 range between 12 and 15. At each of the sites, it is clear that increasing B_1 leads to smaller 80-m wind speeds during regardless of the time of day, although the response is more evident at night. Increasing Pr leads to a smaller wind speed at 80-m height during nighttime but it has nearly no effect on the daytime wind speed. A larger value of α_5 produces larger wind speeds at night while increasing β leads to smaller wind speeds during the day. In contrast to the results in the PBL scheme, the spread of the wind speeds in each bin are much smaller in the surface-layer simulations (rightmost two columns in Fig. 11). This is because most of the variance of the simulated 80-m wind speed are contributed by

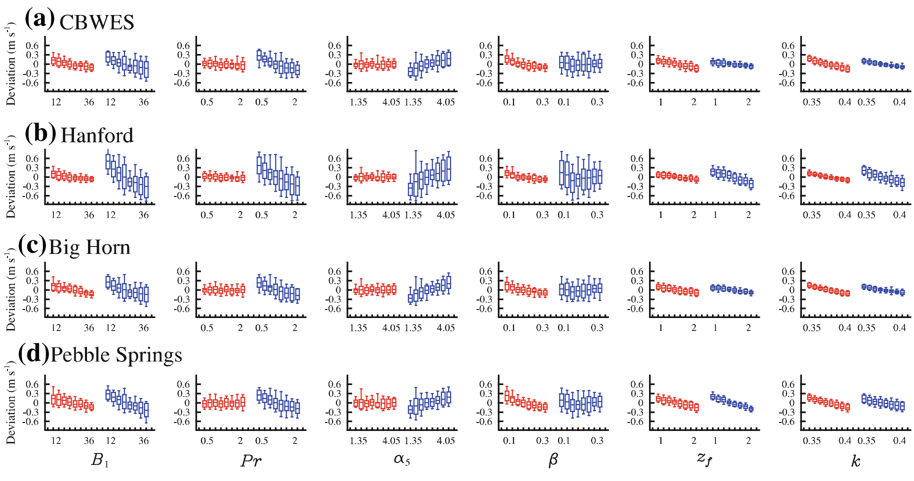

Fig. 11 Averaged daytime (*red*) and nighttime (*blue*) 80-m wind speeds at **a** CBWES, **b** Hanford, **c** Big Horn, and **d** Pebble Springs, in response to the perturbations of the six most influential parameters (indicated at the *bottom* of each *column*) from all the simulations. The 256 simulations in the PBL or surface-layer ensemble are divided into eight discreet bins (each bin with 32 experiments) in terms of each parameter value. In each bin, the mean, 25 to 75th percentile, and 10 to 90th percentile values are presented as box-and-whisker plots. Note that the values are deviations from the respective overall mean of the 256 simulations in the PBL (*left four columns*) or surface-layer (*right two columns*) ensemble

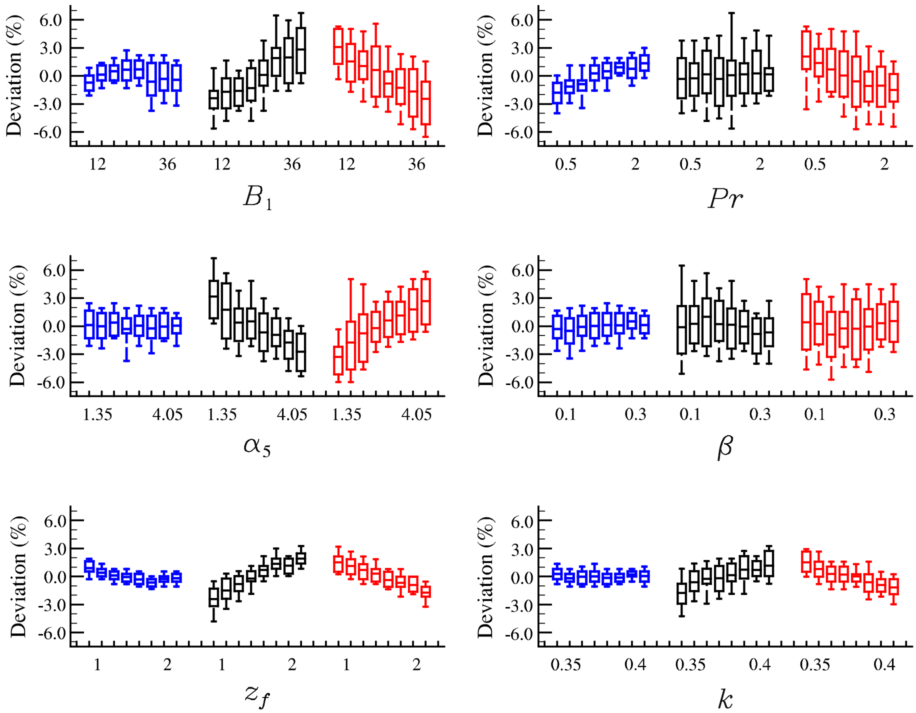

Fig. 12 Frequencies (%) of simulated nighttime 80-m wind speeds of 0–3 m s^{-1} (blue), 3–13 m s^{-1} (*black*), and 13–25 m s^{-1} (*red*) at CBWES, in response to the perturbations of the six most influential parameters from all the simulations. Note that the values are deviations from the respective overall mean of the 256 simulations in the PBL (*top two rows*) or surface-layer (*bottom row*) ensemble

the two most influential parameters of z_f and k. Increasing the value of z_f (i.e., increasing surface roughness) or the von Kármán constant k reduces the wind speed during both day and night. Next, we will explore how the sensitivity changes across different ranges of wind speed. Given the similarity of the results at the CBWES and other sites, our analysis focuses on only the CBWES location.

As the wind power is dependent on the wind speed within certain ranges, we explore the changes in the frequency of occurrence of the 80-m wind speed (at the CBWES site) in three categories, namely 0–3 m s^{-1}, 3–13 m s^{-1}, and 13–25 m s^{-1} based on the cut-in, rated, and cut-out wind speeds of a typical wind turbine, respectively (Fig. 12). It should be noted that situations in which the wind speed is larger than the cut-out speed are not observed in our one-month study period. Our results show that for larger B_1—smaller TKE dissipation rate, the frequencies of wind speeds in the categories of 3–13 m s^{-1} and 13–25 m s^{-1} are markedly increased and reduced, respectively, which implies a reduction in the simulated wind resource. A larger value of Pr reduces the frequency of wind speeds in the range of 13–25 m s^{-1}, increases the frequency of wind speeds in the range of 0–3 m s^{-1}, and causes a very small change in the frequency of wind speeds between 3 and 13 m s^{-1}. This indicates not only a reduction in the simulated wind resource, but also an increase in the frequency of periods with no power production. The effects of larger α_5 are similar to those of smaller B_1, and the impact of β on nighttime wind speed is small, as mentioned earlier.

When the surface roughness is enhanced by increasing z_f, the frequency of occurrence for wind speeds ranging from 0–3 m s^{-1} and 13–25 m s^{-1} is decreased, but increased for wind speeds between 3–13 m s^{-1}, indicating the reduced occurrences of both extremely low and high wind speeds. With increasing k, the occurrence of wind speed in the range 13–25 m s^{-1} is shifted into the range of 3–13 m s^{-1}. This finding could be significant for forecasts of wind-power production given that power is very sensitive to small changes in wind speed within the 3–13 m s^{-1} range, and plateaus once a wind speed of 13 m s^{-1} is reached.

3.2 Vertical Profiles of Wind Speed at the CBWES Site

The vertical profiles of wind speed and the altitude of the nose of the low-level jet (which we have loosely defined as the height, up to 1500 m, at which the maximum wind speed occurs) are analyzed to better understand the evolution of the profile of wind speed. The daytime and nighttime variability of the vertical profile of wind speed at CBWES is shown in Fig. 13. At night, a low-level jet is frequently observed over the site. The WRF model also produces a low-level jet over the CBWES study area, which is consistent with results presented by Yang et al. (2013). The simulations, however, fail to capture the increase in wind speed at an altitude of approximately 300 m at night, which is potentially related to the stretching of the vertical grid spacing and/or the relatively coarse horizontal resolution. In addition, errors could result from biases in the parameter values as they can strongly affect the profile of wind speed (discussed later). Figure 14 shows the diurnal cycle of the wind speed profile above the CBWES site in response to changes in different parameters, along with the ensemble mean fields (contour lines). Because the response of wind speed to the input parameters tends to be monotonic (Fig. 11), the responses of the vertical profile of wind speed to changes in the PBL and surface-layer parameters are summarized as the difference between bin8 and bin1 for each parameter (as defined in Sect. 3.1.2). In contrast to daytime conditions, the mean

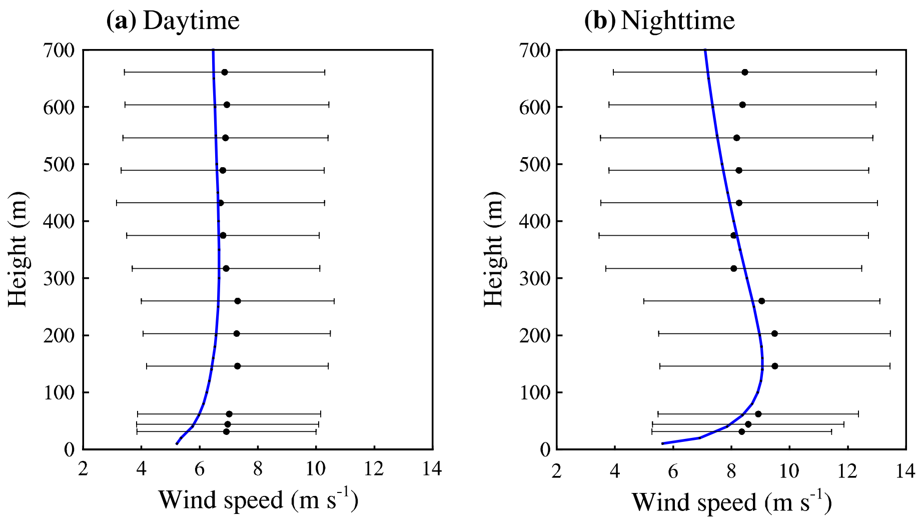

Fig. 13 Vertical profile of observed wind speed (*black dots*) and simulated mean of simulations with perturbed PBL parameters (*blue lines*) during daytime (**a**) and nighttime (**b**) at the CBWES field site. *Black whiskers* denote means ± σ for the observations at each altitude, where σ is the standard deviation (across days) of observed wind speed

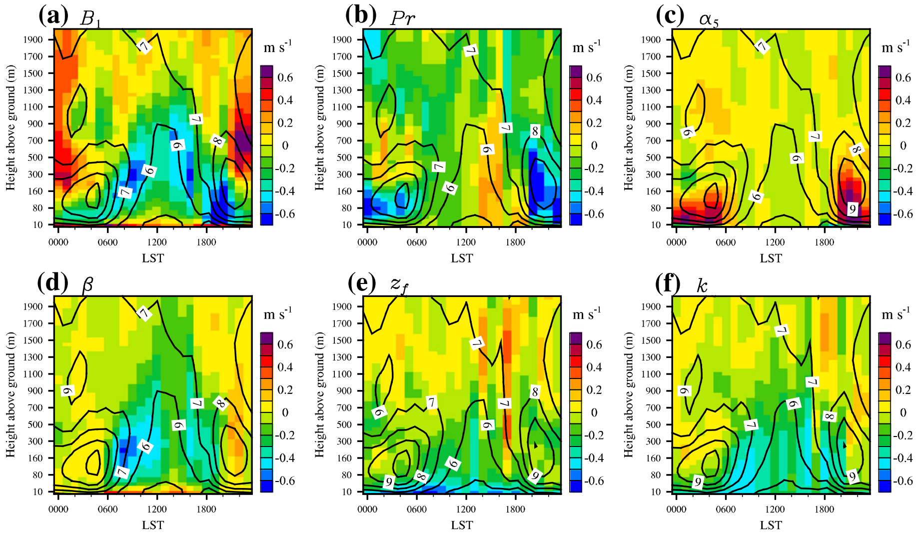

Fig. 14 Diurnal vertical distributions of responses (bin8-bin1 differences, see Sect. 3.1.2) of wind speed (m s^{-1}) at the CBWES field site to the six influential parameters in the PBL and surface-layer schemes. The simulation ensemble means of wind speed (m s^{-1}) in each ensemble are indicated by contours and numbers in the white boxes

wind speed during nighttime is much larger within the lowest 500 m of the atmosphere and is associated with more intense wind shear, which is due in part to the acceleration of hub-height flow by the decoupling of the surface and air aloft. The maximum wind speed at night is around 10 m s^{-1} for heights ranging from 100–200 m above the surface, which is similar to the observations (Fig. 13b). Our results show that the vertical profile of the simulated wind speed can be altered by modifying the parameters in the PBL and surface-layer schemes. The largest differences (colours in Fig. 14) are frequently found to occur at altitudes that span the rotor diameter. During daytime, increasing B_1 leads to larger wind speeds near the surface but smaller wind speeds in the layer above. The figure also highlights the importance of B_1 over the depth of the convective boundary layer (as indicated by the blue colours in panel a). At night, wind speeds are decreased below, and increased above, the nose of a low-level jet.

When Pr is increased, the nighttime wind speed is significantly reduced, especially for altitudes around the jet nose (i.e., 100–300 m above the surface). The situation is reversed in the afternoon, when wind speeds are found to increase within the lowest 1000 m above the surface for larger Pr. As mentioned previously, larger α_5 leads to a larger low-level wind speed at night, especially within the lowest 200 m, while the impact of changing α_5 is negligible during daytime. Increasing β causes weaker daytime wind speeds below 1500 m except for near the surface. Larger wind speeds can be found during nighttime with increasing β. The impacts of parameters z_f and k are similar to each other, and increasing z_f or k causes decreased wind speeds at low altitudes during nighttime and within the daytime convective boundary layer . Similar results of changes in the vertical profile of wind speed in response to varying the parameters are found at the three other sites (figure not shown). These responses are associated with changes in turbulent mixing induced by the perturbations of parameter values and are discussed more thoroughly in Sect. 3.3.

The results shown in Figs. 13 and 14 indicate that the simulated vertical profile of wind speed can be adjusted to better match the observations by parameter tuning. For example, using relatively small values of B_1 or β can reduce the negative biases in the model-ensemble mean wind speeds below 700 m (except for near the surface) during daytime, while using small values of z_f or k can improve the simulated wind speeds in layers both near the surface and aloft. During nighttime, the simulated profile of wind speed can be improved by using small (large) values of $Pr(\alpha_5)$, while using small values of B_1 can produce more agreement with measurement below 200 m but degraded model performance above an altitude of 400 m.

3.3 Turbulent Mixing

The simulated wind fields are mainly affected by parameters via their impacts on the temporal evolution of features of the PBL turbulence. Figure 15 presents time-height cross-sections of the response of the exchange coefficient for momentum to different parameters at the CBWES site. It shows that larger values of B_1 (i.e., smaller dissipation rates of TKE) lead to larger amounts of momentum exchange (Fig. 15a) that are associated with larger TKE values (not shown) during daytime. Because of stronger mixing in the convective daytime PBL, air parcels with large amounts of momentum are transported downwards towards the surface, inducing larger near-surface wind speeds and smaller wind speeds aloft (Fig. 15a). After sunset, because of a decrease in the turbulent mixing associated with larger values of B_1, the surface and layers aloft become quickly decoupled, causing a rapid acceleration of flow above 200 m. Increasing the value of Pr causes weaker vertical transport of heat and less mixing during daytime (Fig. 15b), leading to a weaker diurnal variation of TKE and therefore less acceleration of the wind flow after sunset when the decoupling occurs. Increasing the value of α_5 produces a smaller turbulent length scale at night leading to weaker vertical mixing (Eqs. 8 and 10 in Online Resource 1) and larger low-level wind speeds except at the 10-m height (Fig. 14). Larger values of β increase the turbulent length scale and enhance the vertical mixing during daytime, causing larger wind speeds near the surface and lower

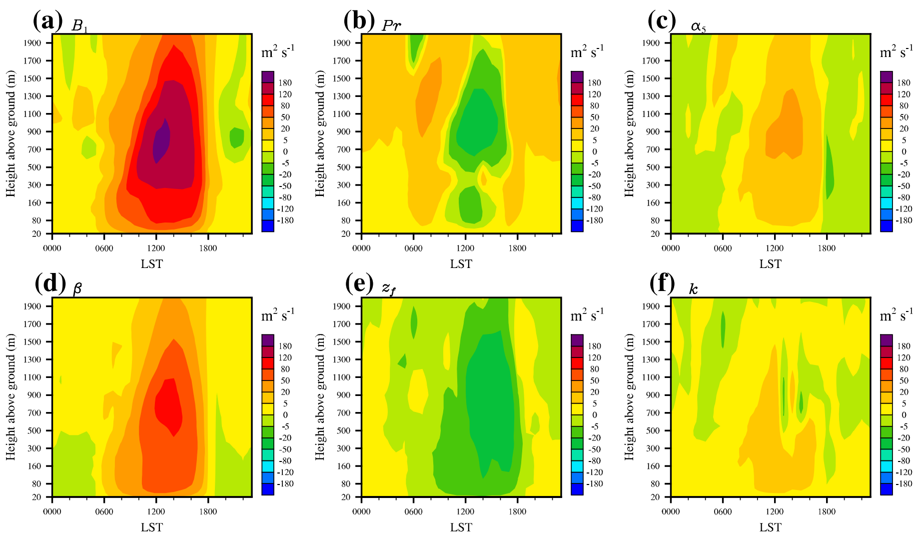

Fig. 15 Diurnal vertical distributions of responses (bin8-bin1 difference) of the vertical exchange coefficient for momentum ($m^2\ s^{-1}$) to different parameters at CBWES

wind speeds aloft. With larger values of z_f, the vertical mixing rate is reduced because of decreased wind speeds associated with increased surface roughness. Similar to β, larger values of k increase the turbulent length scale leading to enhanced vertical mixing during daytime. However, larger values of k also lead to increases in the exchange coefficient for momentum at the surface (e.g. Jiménez et al. 2012), causing reduced wind speeds in layers both near the surface and aloft, which is different to the impacts of β.

4 Summary

We evaluated the sensitivity of WRF-simulated turbine-height wind speeds to a number of parameters used within the PBL and surface-layer parametrization schemes for a domain with complex terrain. An efficient sampling algorithm is used to explore the multiple-dimensional parameter space, and a surrogate model is used to quantify the parametric sensitivity of simulated turbine-height wind speeds. The parameter impacts on the simulated wind shear and turbulence within the PBL are also examined. The results show that perturbing the PBL and surface-layer parameters can have significant impacts on the simulated hub-height wind speed, which in turn leads to a large spread in the predicted wind power. The generalized linear model analysis of the entire study domain indicates that more than 60 % of the variance in the ensemble of simulations are contributed by only six parameters, specifically those related to the TKE dissipation rate, the turbulent Prandtl number, the turbulent length scales in the MYNN PBL scheme, and the surface roughness and von Kármán constant in the revised MM5 surface-layer scheme. The relative contributions of different parameters to total variance are found to be dependent on the terrain slope and stabilities. For example, the turbulent length-scale parameters are generally more important over flat regions where the atmosphere is usually unstable during daytime, and the surface roughness parameter plays more important roles over mountainous areas that also have generally taller and greater coverage of vegetation.

The simulated wind speeds at the CBWES site are explored in detail and compared to observations. The parameter related to the TKE dissipation rate is found to be the most important as it regulates the diurnal evolution of TKE and vertical mixing in the PBL. Increasing the dissipation rate of TKE induces larger hub-height wind speeds, which are favorable for power production. A larger turbulent Prandtl number results in smaller 80-m wind speeds during night, leading to smaller power production as well as an increase in the frequency of wind speed below the turbine cut-in speed. Increasing surface roughness reduces the frequencies of both extremely small and large wind speeds, implying a smaller variability in the hub-height wind speed and more stable power production. Although a single combination of schemes is investigated here, the analyses (e.g. the impact of length-scale parameters on wind speeds) may be transferable to other TKE-based schemes given that the physical underpinnings (e.g. the relationship between turbulent mixing and length scales) are also bases for the parametrization schemes. However, the relative importance of individual parameters can be different due to the differences in the detailed representations within different schemes.

Acknowledgements The authors acknowledge Qing Yang, Hui Wan, Chun Zhao, and William Gustafson Jr. of Pacific Northwest National Laboratory (PNNL) and Joseph Olson of the National Oceanic and Atmospheric Administration (NOAA) for valuable discussions. This study is based on work supported by U.S. Department of Energy's Wind and Water Power program. The Pacific Northwest National Laboratory is operated for the U.S. Department of Energy by Battelle Memorial Institute under contract DE-AC05-76RL01830. Lawrence Livermore National Laboratory is operated by Lawrence Livermore National Security, LLC, for the U.S. Department of Energy, National Nuclear Security Administration under Contract DE-AC52-07NA27344.

The work of B.Y. at Nanjing University is supported by the National Natural Science Foundation of China (41305084). The PNNL Institutional Computing (PIC) and National Energy Research Scientific Computing Center (NERSC) provided computational resources. The NARR reanalysis were freely obtained from CISL Research Data Archive at http://rda.ucar.edu/datasets/ds608.0/. The WRF model outputs used in this study are stored at a PNNL cluster and are available upon request from the corresponding author. Data from CBWES are available from the U.S. Department of Energy Atmospheric Radiation Measurement (ARM) data archive.

References

Andren A, Moeng CH (1993) Single-point closures in a neutrally stratified boundary-layer. J Atmos Sci 50(20):3366–3379

Banta RM, Pichugina YL, Kelley ND, Hardesty RM, Brewer WA (2013) Wind energy meteorology: insight into wind properties in the turbine-rotor layer of the atmosphere from high-resolution Doppler lidar. Bull Am Meteorol Soc 94(6):883–902

Berg LK, Pekour M, Nelson D (2012) Description of the Columbia Basin wind energy study (CBWES). Technical Report PNNL-22036, Pacific Northwest National Laboratory, Richland, Washington, 14 pp

Berg LK, Zhong SY (2005) Sensitivity of MM5-simulated boundary layer characteristics to turbulence parameterizations. J Appl Meteorol 44(9):1467–1483

Boyle JS, Klein SA, Lucas DD, Ma HY, Tannahill J, Xie S (2015) The parametric sensitivity of CAM5's MJO. J Geophys Res 120(4):1424–1444

Businger JA (1988) A note on the Businger-Dyer profiles. Boundary-Layer Meteorol 42(1–2):145–151

Caflisch RE (1998) Monte Carlo and quasi-Monte Carlo methods. Acta Numer 7:1–49

Carvalho D, Rocha A, Gómez-Gesteira M, Santos C (2012) A sensitivity study of the WRF model in wind simulation for an area of high wind energy. Environ Modell Softw 33:23–34

Chen F, Dudhia J (2001) Coupling an advanced land surface-hydrology model with the Penn State-NCAR MM5 modeling system. Part I: Model implementation and sensitivity. Mon Weather Rev 129(4):569–585

Cheng YG, Brutsaert W (2005) Flux-profile relationships for wind speed and temperature in the stable atmospheric boundary layer. Boundary-Layer Meteorol 114(3):519–538

Chou M-D, Suarez MJ (1994) An efficient thermal infrared radiation parameterization for use in general circulation models. NASA Technical Report 104606, 85 pp

Draxl C, Hahmann AN, Peña A, Giebel G (2014) Evaluating winds and vertical wind shear from Weather Research and Forecasting model forecasts using seven planetary boundary layer schemes. Wind Energy 17(1):39–55

Drechsel S, Mayr GJ, Messner JW, Stauffer R (2012) Wind speeds at heights crucial for wind energy: measurements and verification of forecasts. J Appl Meteorol Climatol 51(9):1602–1617

Dyer AJ (1967) The turbulent transport of heat and water vapour in an unstable atmosphere. Q J R Meteorol Soc 93(398):501–508

Dyer AJ (1974) A review of flux-profile relationships. Boundary-Layer Meteorol 7(3):363–372

Fairall CW, Bradley EF, Rogers DP, Edson JB, Young GS (1996) Bulk parameterization of air-sea fluxes for Tropical Ocean-Global Atmosphere Coupled-Ocean Atmosphere Response Experiment. J Geophys Res 101(C2):3747

García-Díez M, Fernández J, Fita L, Yagüe C (2013) Seasonal dependence of WRF model biases and sensitivity to PBL schemes over Europe. Q J R Meteorol Soc 139(671):501–514

Gibson MM, Launder BE (1978) Ground effects on pressure fluctuations in the atmospheric boundary-layer. J Fluid Mech 86(Jun):491–511

Grachev AA, Andreas EL, Fairall CW, Guest PS, Persson POG (2007) SHEBA flux-profile relationships in the stable atmospheric boundary layer. Boundary-Layer Meteorol 124(3):315–333

Grachev AA, Fairall CW, Bradley EF (2000) Convective profile constants revisited. Boundary-Layer Meteorol 94(3):495–515

Grell GA, Dudhia J, Stauffer DR (1994) A description of the fifth-generation Penn State/NCAR Mesoscale Model (MM5), NCAR Technical Note NCAR/TN-398+STR, 117 pp

Guo Z, Wang MH, Qian Y, Larson VE, Ghan S, Ovchinnikov M, Bogenschutz PA, Zhao C, Lin G, Zhou TJ (2014) A sensitivity analysis of cloud properties to CLUBB parameters in the single-column Community Atmosphere Model (SCAM5). J Adv Model Earth Syst 6(3):829–858

Högström U (1988) Non-dimensional wind and temperature profiles in the atmospheric surface-layer: a re-evaluation. Boundary-Layer Meteorol 42(1–2):55–78

Hong S-Y (2010) A new stable boundary-layer mixing scheme and its impact on the simulated East Asian summer monsoon. Q J R Meteorol Soc 136(651):1481–1496

Hong SY, Noh Y, Dudhia J (2006) A new vertical diffusion package with an explicit treatment of entrainment processes. Mon Weather Rev 134(9):2318–2341

Hou ZS, Huang MY, Leung LR, Lin G, Ricciuto DM (2012) Sensitivity of surface flux simulations to hydrologic parameters based on an uncertainty quantification framework applied to the Community Land Model. J Geophys Res 117:D15108

Hu X-M, Klein PM, Xue M (2013) Evaluation of the updated YSU planetary boundary layer scheme within WRF for wind resource and air quality assessments. J Geophys Res 118(18):10,490–10,505

Hu X-M, Nielsen-Gammon JW, Zhang F (2010) Evaluation of three planetary boundary layer schemes in the WRF model. J Appl Meteorol Climatol 49(9):1831–1844

International Energy Agency (2008) World energy outlook: 2008. OECD/IEA

Izumi Y (1971) Kansas 1968 field program data report. Environmental Research Paper, No. 379, Air Force Cambridge Research Laboratories, Bedford, Massachusetts, 86 pp

Jiménez PA, Dudhia J, González-Rouco JF, Navarro J, Montávez JP, García-Bustamante E (2012) A revised scheme for the WRF surface layer formulation. Mon Weather Rev 140(3):898–918

Kim JW, Mahrt L (1992) Simple formulation of turbulent mixing in the stable free atmosphere and nocturnal boundary-layer. Tellus A 44A(5):381–394

Lu X, McElroy MB, Kiviluoma J (2009) Global potential for wind-generated electricity. Proc Natl Acad Sci USA 106(27):10933–10938

Ma PL, Gattiker JR, Liu XH, Rasch PJ (2013) A novel approach for determining source-receptor relationships in model simulations: a case study of black carbon transport in northern hemisphere winter. Environ Res Lett 8(2):024042

Mahoney WP, Parks K, Wiener G, Liu YB, Myers WL, Sun JZ, Delle Monache L, Hopson T, Johnson D, Haupt SE (2012) A wind power forecasting system to optimize grid integration. IEEE Trans Sustain Energy 3(4):670–682

Marjanovic N, Wharton S, Chow FK (2014) Investigation of model parameters for high-resolution wind energy forecasting: case studies over simple and complex terrain. J Wind Eng Ind Aerodyn 134:10–24

Marquis M, Wilczak J, Ahlstrom M, Sharp J, Stern A, Smith JC, Calvert S (2011) Forecasting the wind to reach significant penetration levels of wind energy. Bull Am Meteorol Soc 92(9):1159–1171

Mass C, Ovens D (2010) WRF model physics: progress, problems, and perhaps some solutions. In: The 11th WRF users' workshop, Boulder, CO, 21–25 June, 2010

McCullagh P, Nelder JA (1989) Generalized linear models. Chapman and Hall, London, UK, 532 pp

Mellor GL, Yamada T (1974) A hierarchy of turbulence closure models for planetary boundary-layers. J Atmos Sci 31(7):1791–1806

Mellor GL, Yamada T (1982) Development of a turbulence closure-model for geophysical fluid problems. Rev Geophys 20(4):851–875

Mesinger F, DiMego G, Kalnay E, Mitchell K, Shafran PC, Ebisuzaki W, Jovic D, Woollen J, Rogers E, Berbery EH, Ek MB, Fan Y, Grumbine R, Higgins W, Li H, Lin Y, Manikin G, Parrish D, Shi W (2006) North American regional reanalysis. Bull Am Meteorol Soc 87(3):343–360

Mlawer EJ, Taubman SJ, Brown PD, Iacono MJ, Clough SA (1997) Radiative transfer for inhomogeneous atmospheres: RRTM, a validated correlated-k model for the longwave. J Geophys Res 102(D14):16663–16682

Moeng CH, Wyngaard JC (1986) An analysis of closures for pressure-scalar covariances in the convective boundary-layer. J Atmos Sci 43(21):2499–2513

Musgrove P (2010) Wind power. Cambridge Univ Press, Cambridge, UK, 338 pp

Nakanishi M (2001) Improvement of the Mellor–Yamada turbulence closure model based on large-eddy simulation data. Boundary-Layer Meteorol 99(3):349–378

Nakanishi M, Niino H (2004) An improved Mellor–Yamada level-3 model with condensation physics: its design and verification. Boundary-Layer Meteorol 112(1):1–31

Nakanishi M, Niino H (2006) An Improved Mellor–Yamada Level-3 Model: its numerical stability and application to a regional prediction of advection fog. Boundary-Layer Meteorol 119(2):397–407

Nakanishi M, Niino H (2009) Development of an improved turbulence closure model for the atmospheric boundary layer. J Meteorol Soc Jpn 87(5):895–912

National Renewable Energy Laboratory (2008) 20% Wind Energy by 2030: increasing wind energy's contribution to U.S. electricity supply. U.S. Department of Energy, Washington, D.C., 228 pp

Nielsen-Gammon JW, Hu X-M, Zhang F, Pleim JE (2010) Evaluation of planetary boundary layer scheme sensitivities for the purpose of parameter estimation. Mon Weather Rev 138(9):3400–3417

Paulson CA (1970) The mathematical representation of wind speed and temperature profiles in the unstable atmospheric surface layer. J Appl Meteorol 9:857–861

Pimentel D, Herz M, Glickstein M, Zimmerman M, Allen R, Becker K, Evans J, Hussain B, Sarsfeld R, Grosfeld A, Seidel T (2002) Renewable energy: current and potential issues. Bioscience 52(12):1111–1120

Pleim JE (2007) A combined local and nonlocal closure model for the atmospheric boundary layer. Part I: Model description and testing. J Appl Meteorol Climatol 46(9):1383–1395

Qian Y, Yan H, Hou Z, Johannesson G, Klein S, Lucas D, Neale R, Rasch P, Swiler L, Tannahill J (2015) Parametric sensitivity analysis of precipitation at global and 813 local scales in the Community Atmosphere Model CAM5. J Adv Model Earth Syst 7:382–411

Schumann U, Gerz T (1995) turbulent mixing in stably stratified shear flows. J Appl Meteorol 34(1):33–48

Shaw WJ, Lundquist JK, Schreck SJ (2009) Research needs for wind resource characterization. Bull Am Meteorol Soc 90(4):535–538

Sims REH, Schock RN, Adegbululgbe A, Fenhann J, Konstantinaviciute I, Moomaw W, Nimir HB, Schlamadinger B (2007) Energy Supply. In: Metz Bet al (eds.), Climate Change 2007: Mitigation. Contribution of working group III to the fourth assessment report of the intergovernmental panel on climate change. Cambridge University Press, Cambridge, UK, 851 pp

Skamarock WC, Klemp JB, Dudhia J, Gill DO, Barker DM, Duda MG, Huang X-Y, Wang W, Powers JG (2008) A description of the Advanced Research WRF version 3. NCAR Tech Note NCAR/TN-475+STR, 113 pp

Steeneveld GJ, Mauritsen T, de Bruijn EIF, de Arellano JVG, Svensson G, Holtslag AAM (2008) Evaluation of limited-area models for the representation of the diurnal cycle and contrasting nights in CASES-99. J Appl Meteorol Climatol 47(3):869–887

Storm B, Basu S (2010) The WRF model forecast-derived low-level wind shear climatology over the United States Great Plains. Energies 3(2):258–276

Storm B, Dudhia J, Basu S, Swift A, Giammanco I (2009) Evaluation of the Weather Research and Forecasting model on forecasting low-level jets: implications for wind energy. Wind Energy 12(1):81–90

Stull R (1988) An introduction to boundary layer meteorology. Kluwer Academic Publishers, Dordrecht, 666 pp

Wan H, Rasch PJ, Zhang K, Qian Y, Yan H, Zhao C (2014) Short ensembles: an efficient method for discerning climate-relevant sensitivities in atmospheric general circulation models. Geosci Model Dev 7(5):1961–1977

Yang B, Qian Y, Lin G, Leung LR, Zhang YC (2012) Some issues in uncertainty quantification and parameter tuning: a case study of convective parameterization scheme in the WRF regional climate model. Atmos Chem Phys 12:2409–2427

Yang Q, Berg LK, Pekour M, Fast JD, Newsom RK, Stoelinga M, Finley C (2013) Evaluation of WRF-predicted near-hub-height winds and ramp events over a Pacific Northwest Site with complex terrain. J Appl Meteorol Climatol 52(8):1753–1763

Yang B, Zhang Y, Qian Y, Wu T, Huang A, Fang Y (2015) Parametric sensitivity analysis for the Asian summer monsoon precipitation simulation in the Beijing Climate Center AGCM, version 2.1. J Clim 28(14):5622–5644

Zhao C, Liu X, Qian Y, Yoon J, Hou Z, Lin G, McFarlane S, Wang H, Yang B, Ma PL, Yan H, Bao J (2013) A sensitivity study of radiative fluxes at the top of atmosphere to cloud-microphysics and aerosol parameters in the community atmosphere model CAM5. Atmos Chem Phys 13(21):10969–10987